Flash radiography with 24 GeV/*c* protons

C. L. Morris,[1,a)] E. Ables,[2] K. R. Alrick,[1,b)] M. B. Aufderheide,[2] P. D. Barnes Jr.,[2]
K. L. Buescher,[1] D. J. Cagliostro,[1] D. A. Clark,[1] D. J. Clark,[1] C. J. Espinoza,[1] E. N. Ferm,[1]
R. A. Gallegos,[1] S. D. Gardner,[3] J. J. Gomez,[1] G. A. Greene,[4] A. Hanson,[4] E. P. Hartouni,[2]
G. E. Hogan,[1] N. S. P. King,[1] K. Kwiatkowski,[1] R. P. Liljestrand,[1] F. G. Mariam,[1] F. E. Merrill,[1]
D. V. Morgan,[3] K. B. Morley,[1,c)] C. T. Mottershead,[1] M. M. Murray,[1] P. D. Pazuchanics,[1]
J. E. Pearson,[1] J. S. Sarracino,[1] A. Saunders,[1] J. Scaduto,[5] A. E. Schach von Wittenau,[2]
R. A. Soltz,[2] S. Sterbenz,[1] R. T. Thompson,[4] K. Vixie,[1,d)] M. D. Wilke,[1,3] D. M. Wright,[2]
and J. D. Zumbro[1]

[1]*Los Alamos National Laboratory, Los Alamos, New Mexico 87544, USA*
[2]*Lawrence Livermore National Laboratory, Livermore, California 94550, USA*
[3]*National Security Technologies, LLC, Los Alamos, New Mexico 87544, USA*
[4]*Brookhaven National Laboratory, Upton, New York 11973, USA*

The accuracy of density measurements and position resolution in flash (40 ns) radiography of thick objects with 24 Gev/*c* protons is investigated. A global model fit to step wedge data is shown to give a good description spanning the periodic table. The parameters obtained from the step wedge data are used to predict transmission through the French Test Object (FTO), a test object of nested spheres, to a precision better than 1%. Multiple trials have been used to show that the systematic errors are less than 2%. Absolute agreement between the average radiographic measurements of the density and the known density is 1%. Spatial resolution has been measured to be 200 μm at the center of the FTO. These data verify expectations of the benefits provided by high energy hadron radiography for thick objects. © *2011 American Institute of Physics*. [doi:10.1063/1.3580262]

I. INTRODUCTION

High energy flash X-ray radiography was developed during the Manhattan project in Los Alamos to aid in developing an implosion atomic weapon.[1] The first radiographs of implosions were made in 1944 using bremsstrahlung X-rays from 1 μs pulses of 15 MeV electrons generated by the University of Illinois betatron, which had been transported to Los Alamos. A Wilson cloud chamber photographed with an electronically controlled camera was used to radiograph implosion experiments using spheres of depleted uranium as surrogate cores. These experiments were essential to the development of the implosion bomb tested at Trinity in July, 1945.

After the war, the development of flash radiography continued using the betatron to radiograph static test objects. The goal was to provide quantitative density information for the compressed heavy metal surrogate in non-nuclear implosion experiments (hydro-test experiments) to aid in the design of new weapon systems. Seay[2] developed techniques to reduce X-ray scatter background and record and analyze data that could provide 1% density information for scaled experiments. Venable[3] designed a new pulsed power X-ray machine, PHERMEX, which produced the requisite X-ray dose. Although these techniques were used for a large number of explosively-driven science experiments,[4] the need for them was greatly diminished by the ability to conduct nuclear tests.

The Comprehensive Test Ban Treaty, adopted by the United Nations General Assembly and signed by many nations in 1996, led to a revived interest in the techniques of the 1940s and 1950s. A new set of pulsed power X-ray machines, capable of providing higher doses and shorter pulses than were available from PHERMEX, has been constructed in the US,[5] France,[6] and China.[7] The goal of these new machines is to provide quantitative data from surrogate experiments to certify that nuclear primaries function, using a combination of non-nuclear experiments and large scale super-computer simulations.

Here we demonstrate a new technique, proton radiography, for flash radiography of thick systems, which is superior to X-ray radiography.[8] We present an analysis of data taken during experiment 955 at Brookhaven National Laboratory, using single pulses of 24 Gev/*c* protons provided by the Alternating Gradient Synchrotron (AGS).

The paper is organized as follows. First, we derive a model for the measurement process that incorporates material-dependent effective cross sections and experimental artifacts. Second, we describe the experimental setup and data acquisition. Third, we demonstrate 1% absolute normalization of radiographic images. Fourth, we analyze data from a set of step wedges of materials spanning the periodic table, which we use to fit the model parameters. Fifth, we analyze data from the French Test Object (FTO), a set of nested spherical shells of foam, copper and tungsten, with a maximum areal density of 214 g/cm^2. This analysis demonstrates: 1% agreement with predicted transmission using the model, 1% uncertainty in density reconstruction in a thick object, and 200 μm position resolution.

a)Electronic mail: cmorris@lanl.gov.
b)Deceased.
c)Present address: Johns Hopkins University Applied Physics Laboratory, 11100 Johns Hopkins Road, Laurel, MD 20723, USA.
d)Present address: Washington State University, Pullman, WA 99164, USA.

109, 104905-1

II. OPTIMIZING RADIOGRAPHIC ERROR

A quantitative understanding of the limiting uncertainties of radiography can be obtained from Beer's law.[9] The attenuation of a beam through a given areal density of material, l, in g/cm^2, is described by the exponential equation:

$$N = N_0 e^{-\frac{l}{\lambda}}. \qquad (1)$$

Here, N_0 is the incident number of particles, N is the transmitted number, and λ is the mean free path,

$$\lambda = \frac{A}{\sigma N_A}, \qquad (2)$$

where A is the atomic weight, N_A is Avogadro's number (so that A/N_A is the atomic mass in g), and σ is the absorption cross section. This is a fairly good approximation for high-energy flash radiography with a bremsstrahlung source, where the transmitted flux through a thick object is limited to a band of energies around the minimum in the X-ray attenuation cross section, which occurs at energies near 4 MeV.[10] By assuming perfect detectors and no backgrounds and by assuming that the uncertainty in the transmitted flux obeys Poisson statistics, the uncertainty in the determination of l can be calculated by inverting Eq. (1). In the limit where N is large, the uncertainty is given by:

$$\Delta l = \frac{\lambda}{\sqrt{N}}. \qquad (3)$$

Combining Eqs. (1) and (3), setting the derivative of Δl with respect to λ to zero, and solving for λ gives

$$\lambda = l/2, \qquad (4)$$

the optimum mean free path for radiographing an object of thickness l.

In uranium, the maximum X-ray mean free path is ∼25 g/cm^2 at 4 MeV, which is far from the optimum for hydrotest experiments which are hundreds of g/cm^2 thick. Thus, enormous X-ray machines capable of producing very high fluence are necessary (10 Gy at 1 m from the source) for hydrotest radiography.[5]

An alternative is to use high energy protons. The mean free path for 10–70 GeV protons in uranium is 200 g/cm^2 (Ref. 11) much closer to the optimum given by Eq. (4). Costs of a 20 GeV proton synchrotron designed specifically for hydrotest radiography[12] are comparable to the DARHT X-ray facility (construction costs for the two DARHT axes summed to about $500M).[13] Proton Radiography is currently being used for radiography of thinner/less dense dynamic systems both at Los Alamos, using the 800 MeV Los Alamos Neutron Science Center accelerator (LANSCE),[8] and in Protvino, Russia, using the U70 accelerator.[14] New facilities are being constructed in Germany[15] and China.[7] In this paper we present the first quantitative experimental assessment of high-energy proton radiography for thick objects.

III. CHARGED PARTICLE INTERACTIONS

In proton radiography, the attenuation of a beam of protons passing through an object is measured by focusing the transmitted beam with a set of quadrupole magnets onto an image plane detector. To a good approximation, the interaction of energetic charged particles with matter can be factored into three parts: the Coulomb interaction with the electrons in the medium, the Coulomb interaction with the atomic nuclei, and the strong nuclear interaction with the atomic nuclei. The first two of these interactions can be described using the Rutherford scattering cross section and two-body kinematics. The nuclear interaction can be parameterized to good precision using simple geometric models.

Coulomb scattering of the incident charged particle from the electrons in the object leads to continuous energy loss. This is the result of many two-body interactions that, in the laboratory frame, result in small momentum changes to the incident particle but relatively large energy transfers to the lighter electrons. The mean value of the energy loss is well described by the Bethe-Bloch formula.[16]

Because the energy loss is the result of many individual collisions, the process is stochastic. Fluctuations occur in both the number of collisions and the energy loss in each collision. The distribution of energy loss differs from a Gaussian because of a tail on the large energy loss side of the distribution. Landau[17] was the first to derive a more accurate distribution that included the tail from high energy loss collisions. This work was further refined by Vavilov.[18]

Energy loss results in charged particles slowing down and stopping in matter. The Bethe-Bloch formula can be integrated to determine the range of charged particles in matter. The energy loss fluctuations result in a distribution of ranges. A $1/v^2$ rapid rise in the nonrelativistic region of the Bethe-Block formula leads to a peak in the energy loss distribution at low energy, which is known as the Bragg peak.

Coulomb scattering from the atomic nuclei is similarly described by integrating the results of individual collisions between the incident particle and nuclei in the matter. The mass ratio in these collisions leads to direction changes in the beam particles. The screened Coulomb cross section is large, so that the mean free path between collisions is small. For finite thickness objects, the angular distribution on passing through matter generally involves the convolution of many collisions.

Large Coulomb cross sections (small mean free paths) combined with small momentum transfers per collision lead to a Gaussian angular distribution for high-energy beams of charged particles traversing finite thickness foils. The theory for multiple Coulomb scattering was first derived by Fermi.[19,20] More exact treatment of the tails, which result from small numbers of large angle scatters, was first considered by Moliere,[21,22] then refined by Bethe[23] and later authors. Gaussian approximations, which reproduce the variance due to the tails, have been studied by Highland[24] and more recently Lynch and Dahl.[25]

The strong nuclear force leads to nuclear scattering. The nuclear cross section includes both elastic and inelastic terms. For elastic scattering, the nucleus is left in its ground state. In this case, the energy transferred to the nucleus can be calculated using two-body kinematics. In a simple approximation, elastic scattering results from the wave diffraction due to the flux removed from the incident beam by a

black disk with the nuclear radius, and inelastic scattering is the shadow of the black disk.[26] In this geometric model the total elastic cross section, σ_E, is approximately equal to the total inelastic cross section, σ_I, and both of these are given by:

$$\sigma_E = \sigma_I = \pi r^2. \tag{5}$$

The nuclear radius depends on A, the atomic weight, approximately as: $r = r_0 A^{1/3}$, where $r_0 = 1.2$ fm.[27]

Empirical fits to high energy nuclear scattering data preserve the form of the black-disk model, but vary the size and the A dependence for these two processes. A good empirical estimate of the cross sections and mean free paths is given in the Particle Data Review.[28]

IV. RADIOGRAPHY WITH CHARGED PARTICLE BEAMS

Koeler[29] was the first to publish proton radiographs, which were taken with 160 MeV protons provided by the Harvard cyclotron. These relied on the high contrast that could be obtained by using protons at the end of their range using the Bragg peak. Koeler showed that very high contrast radiography could reveal details that were not visible in X-radiography, but the position resolution was limited by multiple scattering of the protons.

Wilson[30] demonstrated a new form of radiography using high energy protons that relied on multiple Coulomb scattering, which led to edge enhancement due to the position-dependent blur function near edges. The medical uses of proton radiography formed the basis for many early studies.[29–40] However, poor position resolution, due to multiple Coulomb scattering, and high cost have limited the practical applications of radiography with low energy protons.

In this paper we study the use high-energy proton beams for radiography. In this case, contrast is achieved by the removal of the beam due to nuclear and Coulomb interactions in the target. Here, we use magnetic lenses to focus the beam transmitted through the target onto imaging detectors.

A simple, elegant magnetic lens is described by Mottershead and Zumbro.[41] It provides coplanar, unit magnification imaging, as well as a Fourier plane in the mid plane of the lens. With this system, the contrast of the image can be controlled by changing the solid angle, Ω_L, of the beam passed by a collimator at the Fourier plane. The position resolution is determined by chromatic aberrations, to first order. These are minimized by preparing an illuminating beam with a position-angle correlation that causes the two lowest order chromatic terms to cancel.[41] Image blur can be reduced to any desired level by increasing the beam momentum to reduce multiple scattering and fractional energy spread.

The transmission of particles through the object and lens system can be approximated if the scattering is factorized into a single- and multiple-scattering piece. In this approximation, inelastic scattering is assumed to result in large energy loss and scattering angle so that these particles are outside of the lens acceptance, Ω_L. Elastic scattering also contributes to the removal cross section of particles that are scattered outside of the lens acceptance in a single collision.

The removal cross section, σ_{RM}, for an object of a single material is given by:

$$\sigma_{RM} = \sigma_I + \int_{4\pi - \Omega_L} \frac{d\sigma_E}{d\Omega} d\Omega. \tag{6}$$

The elastic contribution is expressed as an integral over the solid angle not accepted by the lens, Ω_L, in order to avoid the singularity of the nonintegrable Coulomb cross section at forward angles.

If the angular acceptance of the lens is large compared to the Coulomb multiple scattering angle of the object being radiographed with areal density, l, the attenuation, $t_\lambda = N/N_0$, is exponential and given by

$$t_\lambda = e^{-l/\lambda}, \tag{7}$$

where, as above, N_0 is the incident flux, N is the transmitted flux, and

$$\lambda = \frac{A}{\sigma_{RM} N_A}. \tag{8}$$

The integral in Eq. (6) leads to an effective nuclear attenuation length that depends on the collimator angle.

If the lens acceptance cuts into the multiple scattering-angular distribution, there is another contribution to the attenuation due to multiple scattering. In order to calculate this contribution, we assume that the multiple scattering polar-angular distribution is Gaussian:

$$\frac{dN}{d\theta} = \frac{1}{2\pi\theta_0^2} e^{-[\theta^2/(2\theta_0^2)]}, \tag{9}$$

the Fermi approximation discussed above, where θ is the polar angle and θ_0 is the multiple scattering angle given approximately by:

$$\theta_0 = \frac{14.1\text{MeV}}{p\beta} \sqrt{\frac{l}{X_0}}. \tag{10}$$

The proton momentum and velocity are p and β, respectively, and X_0 is the radiation length for the material. In the case where the angular acceptance of the lens is defined by a constant polar angle, θ_c, the transmission, t_X, is obtained by integrating the fraction of the angular distribution that lies within the lens acceptance,

$$t_X = \int_0^{\theta_{CC}} \frac{1}{2\theta_0^2} e^{-[\theta^2/(2\theta_0^2)]} \sin(\theta) d\theta \approx 1 - e^{-\kappa/l}. \tag{11}$$

The length scale, κ, for multiple-scattering radiography,

$$\kappa = \left(\frac{p\beta\theta_C}{14.1\text{MeV}}\right)^2 \frac{X_0}{2}, \tag{12}$$

is independent of l but dependent on the material, through X_0, a material parameter. The approximations made in estimating t_X are expected to be good for thick objects (as verified by the step wedge data below), where the multiple scattering is well described by a Gaussian distribution. The

total transmission, t, is just the product of the nuclear attenuation from Eq. (7) and the multiple-scattering transmission through the collimator from Eq. (11):

$$t = t_\lambda t_X. \tag{13}$$

An error analysis can be performed by taking the derivative of Eq. (11) with respect to l:

$$\frac{dt_X}{dl} = \frac{\kappa}{l^2} e^{-\kappa/l}. \tag{14}$$

The relative uncertainty in the measurement of l is:

$$\frac{\Delta l}{l} = \frac{l}{\kappa} \frac{\sqrt{t_X}}{1 - t_X} \frac{1}{\sqrt{N_0}}, \tag{15}$$

where the uncertainty in the measurement of transmission is assumed to be statistical only. Eq. (15) can be solved for a minimum as a function of κ as with Eq. (3). The result is $\kappa = 0.644 \, l$. The relative size of the uncertainty for a given incident flux, N_0, is about a factor of 1.5 larger than for transmission radiography alone (for $\kappa = \lambda$). In addition, the size of the uncertainty grows more rapidly for small l and more slowly for large l than for attenuation radiography. This is plotted as the dotted curve in Fig. 1.

The effect of beam emittance and overburden material (windows, air, etc.) on the transmission can be included in this Gaussian approximation by adding the additional contribution to the beam divergence referenced to the target location, a, normalized to units of κ, in quadrature to the multiple scattering caused by the object. This gives:

$$t = e^{-l/\lambda_\theta} \frac{1 - e^{-\kappa/(l+a)}}{1 - e^{-\kappa/a}}. \tag{16}$$

In this expression, the denominator accounts for the attenuation of the beam due to emittance and overburden when there is no object, and N_0 is measured in the object plane of the lens. The relationship between the divergence of the beam, θ_b, and the parameter a is:

$$a = \frac{X_0}{2} \left(\frac{\theta_b p \beta}{14.1 \text{ MeV}} \right)^2. \tag{17}$$

In the step wedge fits, below, we will parameterize X_0, and fit for the effective beam emittance, θ_b.
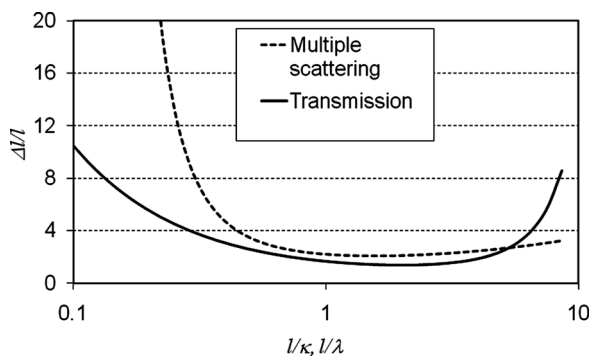

FIG. 1. Relative uncertainty in the radiographic determination of thickness ($\Delta l/l$) for transmission and multiple-scattering radiography as a function of the dimensionless thickness.

V. EXPERIMENT

Here, we present an analysis of data taken on a thick test object to demonstrate flash radiography with an energetic proton beam. The beam consisted of single pulses of 24 GeV/c protons provided by the Alternating Gradient Synchrotron (AGS) at Brookhaven National Laboratory. A beam line with a matching section and magnetic lens was constructed for these experiments,[41] as shown in Fig. 2. Beam extracted from the AGS was transported to the U-line area with the Relativistic Heavy Ion Collider (RHIC) insertion line. A dipole magnet that would normally bend the beam into the RHIC insertion line was turned off, allowing the beam into the U-line. A series of trim dipoles and quadrupoles was used for the final tune of the beam into the proton radiography area.

The beam extracted from the AGS was focused onto a 1.2 cm-thick tantalum diffuser (located at the left side of Fig. 2). The beam momentum spread at this point was on the order of 0.1%, based on the known AGS emittance. A pair of quadrupole magnets upstream of the target location was used to prepare the beam at the target with a position-angle correlation that matched the beam to the chromatic length of the imaging lens. The lens consisted of 8 quadrupoles, 20 cm diameter, 120 cm long, that were configured to form a unit magnification imaging lens.[41] Either of a pair of collimators, 1.2 m long right circular cylinders of tungsten, was located at the Fourier midplane of the lens. The collimators approximated multiple-scattering angle acceptance cuts, θ, of 4.56 and 6.68 mrad.

A set of step wedges and a test object, the French Test Object (FTO), was radiographed using pulses of up to 3×10^{10} protons with a pulse length of 30–40 ns. A single beam pulse was sufficient to make a 2D radiograph of the FTO.

Optical images of the transmitted beam in the image plane of the magnetic lens were formed on a 2.0 mm thick LSO tiled scintillator plate. The optical image was relayed to two independent CCD-based camera systems, one an ungated 1600×1600 Pixel Vision™ back illuminated CCD camera, and the other a channel plate gated custom-built CCD camera. The analysis presented here uses the images from the Pixel Vision™ camera. The field of view was about 12×12 cm^2, and a camera pixel corresponded to about 75 μm at the object. A transformation between positions at the object and image locations was obtained by imaging a block of aluminum with a grid pattern machined into it. A second order two-dimensional polynomial that mapped the positions of the intersections of the grid measured in the image plane to the known locations in the object plane was fitted to the data using least squares. The root mean square of the residuals obtained for 55 points spread over the image plane was 29 μm.

The intensity of each beam pulse was monitored at the diffuser location, at the collimator location, and at the image location, in a set of three Bergoz coils[42] that were calibrated to absolute charge with current loops. These output signals were recorded with digital oscilloscopes and integrated to provide the proton intensity for each beam pulse. The
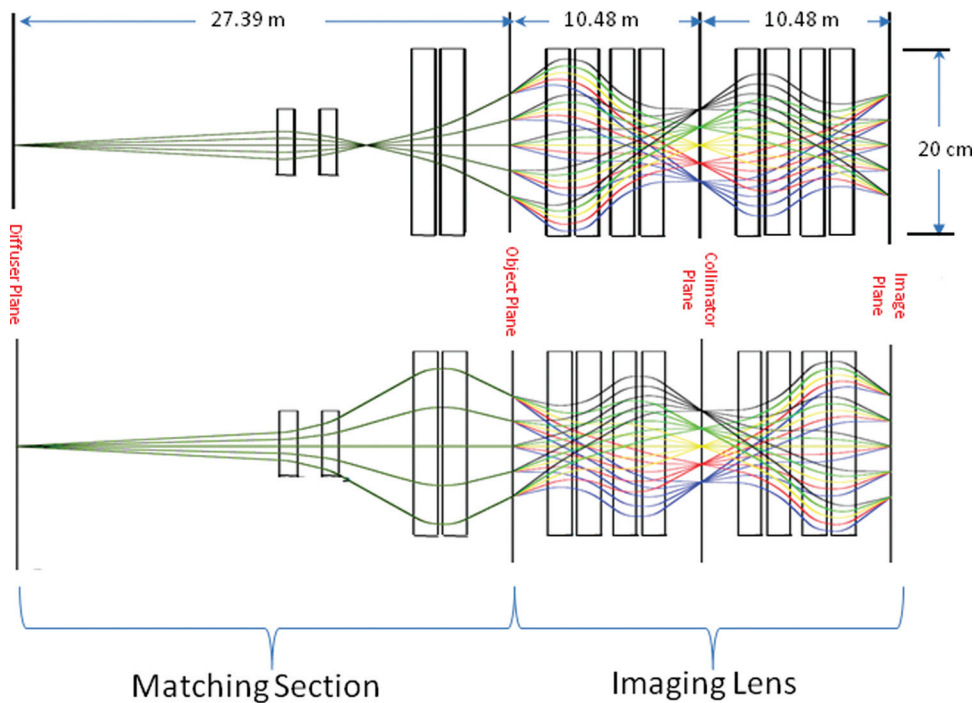
FIG. 2. (Color) Layout of the lens system used for the measurements reported here. The rays from the diffuser are separated by 1 mrad of scattering; the rays from the object are also separated by 1 mrad of scattering. Note the exaggerated vertical scale.

relative precision of these measurements was determined to be ∼1.5% by comparing the three measurements for multiple beam pulses under similar conditions.

A plot of the integrated CCD image plane camera output versus the Bergoz coil measurement is presented in Fig. 3. These measurements demonstrate the linearity of the imaging system to ∼1% up to a beam fluence of ∼5×10^{10} protons per image. The gain residuals from the fit appear to be random and have been used to estimate that the precision of the fluence measurements from the camera images is 1.3%. This dynamic range covers the range of the data presented below.

Other digital video cameras (Pulnix TM-1040[43]) viewed the beam at two positions upstream of the diffuser location and were used to monitor the incident beam position and angle in both the horizontal (x) and vertical (y) planes. The position of the beam on the diffuser was calculated as a linear function of the measured position of the incident beam in these upstream monitors. Coefficients of the first order polynomial were fitted to a large set, over 600, of beam pictures taken during the course of the experiment. These results are plotted in Fig. 4. These fits were used to correct for shifts in the incident beam position with a precision of about 0.5 mm; the root mean square (rms) of the fit to the horizontal positions is 0.63 mm and in the vertical direction is 0.51 mm. This procedure was used to analyze the test object data (described later), but not the step wedge data, since the Pulnix camera data were only available for the later part of the experiment. The nonuniform distributions reflect discrete changes in the beam tune.

A. Camera calibration and data reduction

Camera data were processed by the following steps, described below: dark subtraction, star removal, scintillator background correction, gain/fixed pattern noise correction, and beam flattening.

Camera dark signal was subtracted from each picture. Stars induced by nuclear interactions of background radiation in the CCD were filtered by identifying outlying pixels and replacing each of them with a median of the pixels on the perimeter of a surrounding square.[44] Outliers (typically < 1% of the pixels) were pixels that were more than three standard deviations away from the median of the surrounding pixels. In this analysis the perimeter of the square was 64 pixels long. Because we perform least-squares fitting, below, our results are not sensitive to the variance reduction caused by this procedure. In any case, the impact would be negligible because of the small fraction of pixels affected.
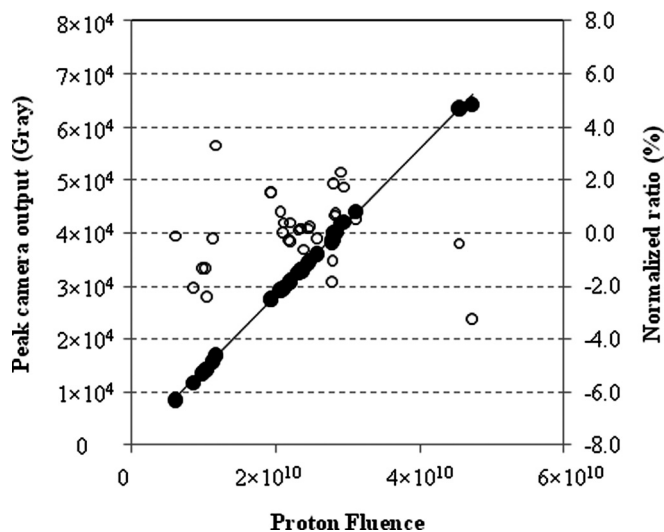

FIG. 3. (Left axis) Peak light output of the camera LSO system versus proton fluence (solid points), and linear fit (solid line). (Right axis) Camera gain (ratio of proton fluence to light output), plotted as the deviation from the average gain, versus proton fluence.
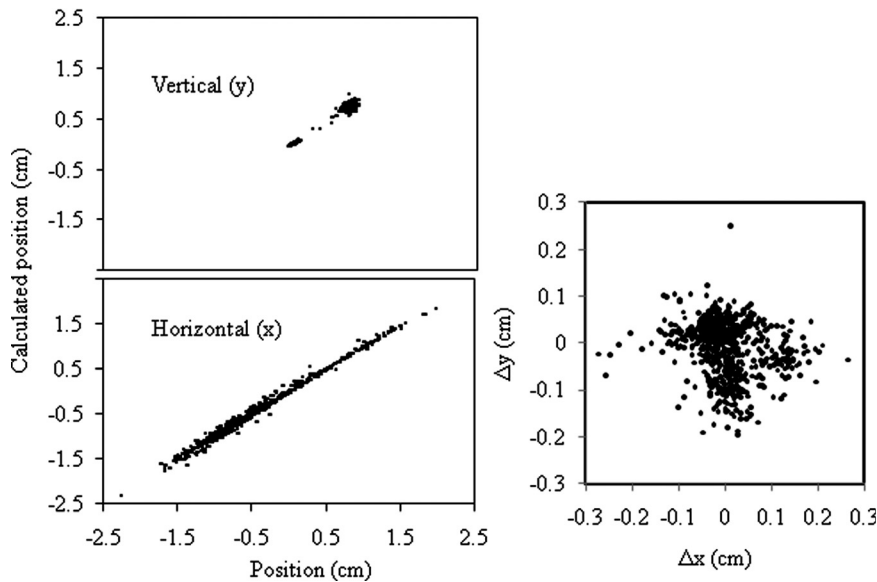
FIG. 4. (Left) Calculated beam position at the image plane from the Pulnix cameras versus measured beam position in the image plane. (Right) The residuals from the fit shown on the left.

In addition to the image, the scintillator was found to produce diffuse light whose intensity was proportional to the total light produced by a given tile, but whose position distribution was uniform. This was measured using a pencil beam and comparing the background level of light with the total amount of light. The background (tile glow) was 5% of the integrated light on each tile and was accordingly subtracted from each image.

Multiple beam pictures were fitted with two-dimensional Gaussian curves. Ratios of the fit to the data were averaged and were used to correct the camera data for fixed pattern noise. This is effectively a per-pixel gain correction, which was generally <10%.

The beam profile was removed from each picture by assuming the beam profiles were Gaussian in shape. We fitted a two-dimensional Gaussian to the regions outside of the object. The width of the Gaussian was constrained to the value obtained from the beam fits. We then divided the image by the Gaussian to obtain the final corrected transmission image.

Finally, for convenience in later analysis, we resampled the images using a 10 sample Monte Carlo average to obtain a 100 μm pixel scale. While this does reduce the per-pixel variance, it does not impact the least-squares fitting procedure, as discussed below.

B. Step wedge calibration data

Step wedges were imaged to obtain transmission as a function of thickness for eight materials: beryllium, carbon, aluminum, iron, copper, tin, tungsten, and lead. A photograph of a set of step wedges in the object location and a processed radiographic image are shown in Fig. 5. These materials were chosen so that our parameterization (see below) would span the periodic table. The aluminum and tungsten were alloys of unspecified composition but known density. The aluminum was treated as a pure material. The tungsten was assumed to have a composition that was 90% tungsten and 10% iron by weight. The size of each step was 10.16 mm $\times$ 12.7 mm.

Transmission as a function of thickness was obtained by averaging the measured transmission over a 25 mm^2 region where the transmission was flat (50×50 pixels) for each step. (Typically, the transmission in the region varied by less than 1% of the average.) Results for the step wedges are shown in Fig. 6.

The lines show least-squares fits to the data using Eq. (16).

In the fit, the X_0 were parameterized by:

$$X_0 = \frac{a_X A}{Z(Z+1) \ln\left(b_X/\sqrt{Z}\right)},\qquad(18)$$

a parameterization attributed to Dahl,[28] and (combining Eqs. (5) and (8)) the λ_θ were parameterized as:

$$\lambda_\theta = a_\theta A^{b_\theta},\qquad(19)$$

for collimator angles, θ, of 4.56 and 6.68 mrad. Here A and Z are the atomic weight and the atomic number, respectively. The material dependence is entirely contained in the A and Z in Eqs. (18) and (19).
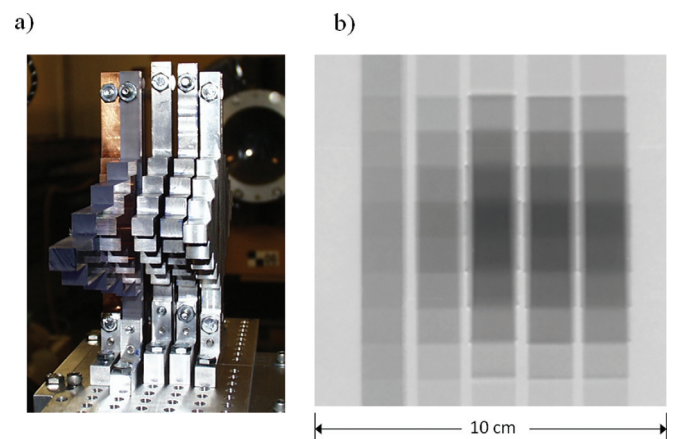
a)   b)

FIG. 5. (Color) (Left) photograph of step wedges in the object location. (Right) proton transmission radiograph of the step wedges.
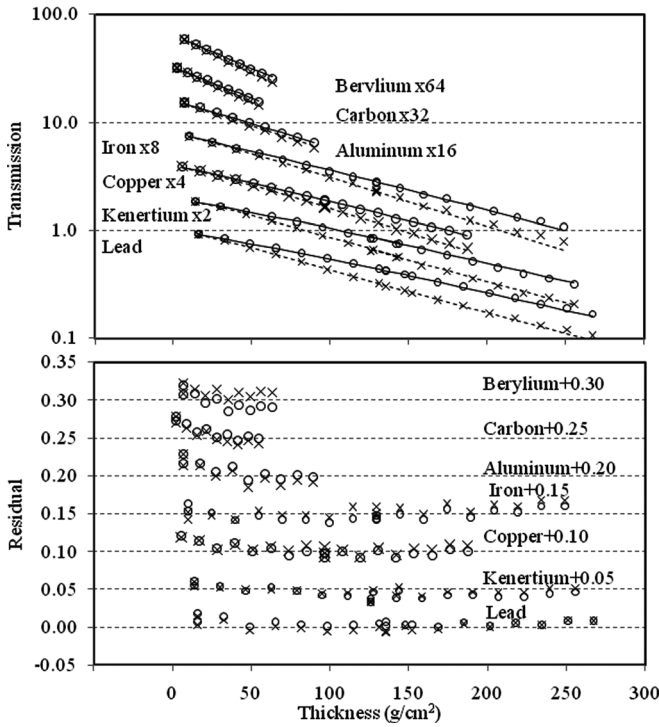
FIG. 6. (Top) Measured transmission as a function of thickness for the step wedge data. The lines are fits to the data using Eq. (16). The circles and solid lines are taken with a 6.68 mrad collimator and the x's and dashed lines are with a 4.56 mrad collimator. (Bottom) The residuals.

In this fit, the independent parameters are $l_{i,j}$, the areal density of each step j of each material i. The dependent parameters are the measured transmissions $t_{i,j}$ through each step. The material properties A_i and Z_i, the beam momentum $p\beta$, and the collimator cut angles θ_1 and θ_2 are taken as known constants. This leaves seven parameters to fit: the four collimator-dependent cross section parameters a_θ, b_θ, from Eq. (19); the two radiation length parameters a_X, b_X, from Eq. (18); and the beam divergence, θ_b, from Eq. (17).

The results of the fit are given in Table I. The rms residual of the fit transmissions over both collimator angles and all materials is 0.9%. Uncertainties for the fit parameters were estimated using this rms as the uncertainty for the measurements. (This assumption prevents us quoting a goodness of fit statistic, such as χ^2.) The uncertainties are incomplete, as no attempt has been made to fully evaluate all of the systematic errors in the step wedge analysis.

The results for λ approximately follow the expectation based on the geometric model discussed above. The simple geometric model would have given $a_\theta = 37$ g/cm^2 and $b_\theta = 1/3$ for collimator angles large enough to accept the

TABLE I. Fitted parameters for the radiation length and attenuation length parameterization.

Collimator	a_θ [g/cm^2]	b_θ
4.56 mr	28.36 ± 0.02	0.3580 ± 0.0003
6.68 mr	35.06 ± 0.03	0.3182 ± 0.0003
a_X	230.1 ± 2.1 g/cm^2	
b_X	34.5 ± 0.5	
θ_b	1.05 ± 0.02 mr	

elastic scattering, $\theta > kr\theta > kR$, where k is the proton wave number and r is the nuclear radius. This corresponds to angles $\gg 1$ mrad, for high Z nuclei. In our case, the nuclear attenuation length also depends on collimator angle. This is due to the angular dependence of the elastic scattering contribution to the removal cross section (see Eq. (6)).

We note that this parameterization gives radiation lengths (X_0) that are significantly different from the standard values, $a_X = 716.4$ g/cm^2 and $b_X = 287$. This may be due to contributions of plural nuclear scattering to the Coulomb multiple scattering distribution, which is not included in the Gaussian approximation used here. The angle cutoff provided by the right-circular cylinder collimator geometry is not sharp and the collimator angles, based on first order magnetic optics, are only approximate. The effect of the finite length of the collimator has been considered more thoroughly in previous work, where it is shown that more complex collimator geometries can provide sharper angle cuts.[45,46] Here we used an empirical approach to deal with this issue.

C. French test object results

We have taken data on a thick test object, the so-called French Test Object (FTO). The FTO is a standard object used to compare radiographic capability among flash X-ray machines. The FTO consisted of three concentric spherical shells; the inner was machinable tungsten (Kennertium®) with an inside radius of 1 cm and an outside radius of 4.5 cm. Kennertium is a sintered tungsten alloy containing small amounts of nickel, iron and copper. This was surrounded by a copper shell of outside radius of 6.5 cm, and this was surrounded by a shell of foam plastic with an outside radius of 22.5 cm. The FTO presents a maximum areal density of 214 g/cm^2. The Kennertium shell is not expected to have a uniform density to better than several percent.

The FTO is larger than the 12 cm radiographic field of view. The data were analyzed using the predictions of the beam center and shape obtained from the upstream measurements of the incident position and angle, as previously described. The fluence normalization was obtained by using the proton intensity measured in the Bergoz coils. A transmission radiograph obtained in this manner is shown in Fig. 7.

A forward model prediction of the transmission using the fitted step wedge parameters is shown in Fig. 8. The residuals are a few times 0.1%, except near material boundaries, where finite resolution effects and alignment errors between the data and the model lead to larger residuals. There is a systematic difference between the two sets of data at different collimator angles. Transmission with the 6.68 mrad collimator is under-predicted relative to the 4.56 mrad collimator. We do not understand this but speculate it is due to unaccounted for backgrounds (discussed below).

In order to study the precision for reconstructing densities, the transmission radiographs were divided by a prediction of transmission through the two outer shells (foam and copper) and Eq. (16) was used to solve for the areal density. The step wedge parameterization along with measured material densities and shell geometry were used to calculate the transmission through the overburden (the outer two shells).
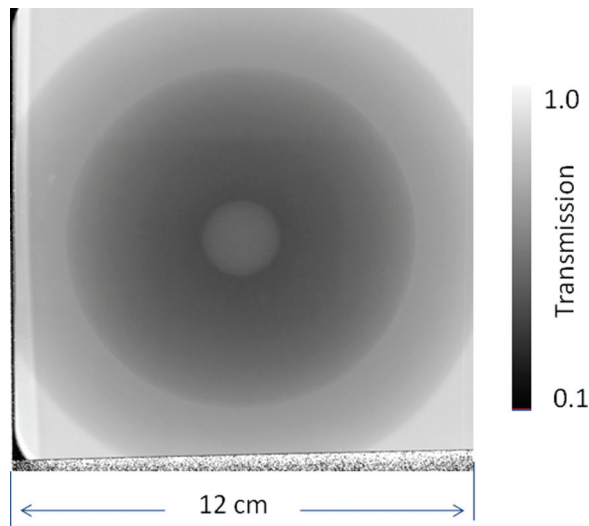
FIG. 7. (Color online) FTO radiograph corrected for fixed pattern noise and divided by the beam shape. Transmission is plotted on a logarithmic scale.
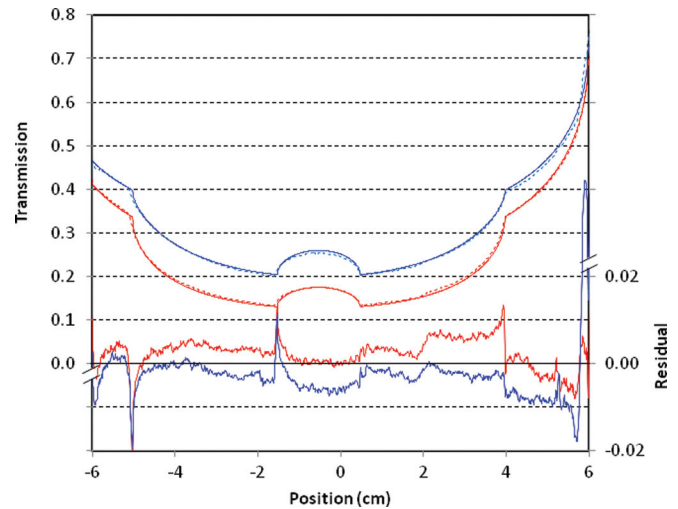

FIG. 8. (Color) FTO data (dashed lines) model (solid lines) and the residuals. The red curves are for the 4.56 mrad collimator and the blue curves are for the 6.68 mrad collimator. The curves correspond to projections through the center of the radiographs.

The overburden was included in the beam divergence parameter a. Axial symmetry was assumed and a regularized[47] Abel inversion[44] was then applied to the areal density to obtain volume density. Images obtained at each step in the density reconstruction are shown in Fig. 9.

Five separate images of the FTO were taken under the same conditions. The average incident proton dose for these images was 2.7×10^{10}, spread over a beam spot with a Gaussian width (σ) of about 5.2 cm. Comparing these allows an estimate of the reproducibility of the radiographic procedures, including uncertainties in the beam position and intensity measurements. A plot of the volume densities measured for a single stripe of 100 μm voxels on a line through the center of the object is shown in Fig. 10.

The figure shows the reconstructed density along a single row of 100 μm voxels through the center of the FTO, as well as the per-voxel rms deviation across the five runs. In the interval between -4 and -2 cm (200 voxels) the rms deviation is generally about 5%. Although the variance in individual voxels is dominated by statistical uncertainty, there are variations in the average density on the order of 2% that are not statistical. The standard deviation of the five image average value on this interval is 0.7%, whereas we would expect 0.16% from averaging 200 voxels times five images each with 5% error. The 0.7% rms is consistent with the uncertainty in the measurement of the proton fluence. The

average measured density of 18.1 ± 0.2 g/cm^3 is within 1% of the conventionally measured density of the Kennertium shell of 18.28 ± 0.04 g/cm^3. The average was taken of the same 200 voxels and all five images.

Spatial resolution in proton radiography is determined by multiple scattering due to material in the proton path between the object and image planes of the lens, chromatic aberrations, and the optical resolution of the imaging system.

The edge of the cavity in the center of the FTO was fitted with an error function plus a constant in order to determine the edge resolution near the center of the object. These results are shown in Fig. 11. The fit gave a value of 200 ± 10 μm for the Gaussian width (σ) of the error function. This includes a negligible contribution due to the smoothing introduced by the regularization of the Abel inversion, but the damping factor was set, by trial and error, so as to increase the resolution by less than 10%. In the fit some residual background (5%) in the cavity region is evident. We speculate that this is due to unidentified background in the transmission radiograph but have not investigated this further. The limiting resolution, estimated using a forward model to predict a radiograph[44] that was run though the same analysis chain as the data, was estimated to be 100 microns. The difference between the measured and predicted resolution is likely to be due to imperfections in the proton magnetic and
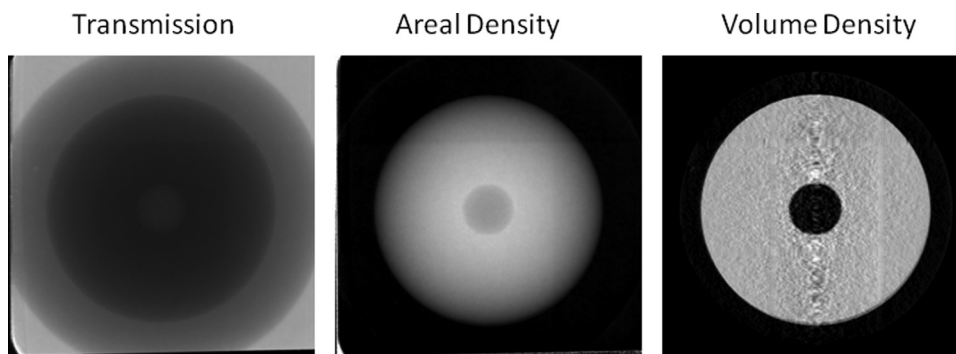

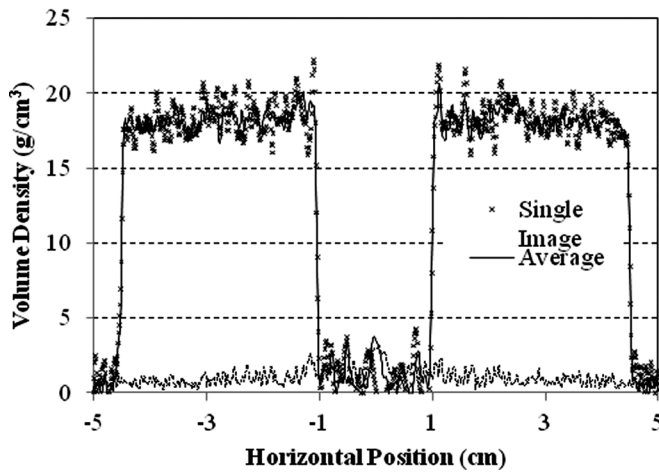FIG. 9. Images of the steps in the density reconstruction.

FIG. 10. Plot of the reconstructed densities on a horizontal line through the center of the FTO. The points marked with x's are for a single image, the solid line is an average obtained from 5 images and the dashed line is the standard deviation of each point for the five images.

the photon detector optics that were not accounted for in the forward model.

VI. CONCLUSIONS

Radiographic data using short pulses of 24 GeV/*c* protons provided by the Brookhaven National Laboratory AGS have been presented. We have shown techniques for measuring the beam intensity and position that allow the radiographic transmission to be normalized absolutely to 1%. A global model fit to step wedge data is observed to give a good description spanning a wide range of atomic numbers and object thicknesses. The parameters obtained from the step wedge data were used to predict transmission through the FTO to a precision better than 1% in 100 μm pixels. Volume density reconstructions have been performed. Multiple trials have been used to show that the systematic errors are ~2% on 100 μm voxels. The average absolute measured radiographic density agrees with the known density within 1%. Position resolution has been measured to be 200 μm at the center of the FTO. These data verify the expectations of the benefits offered by high-energy hadron radiography for thick objects. Although the precision and position resolution demonstrated here are by no means the limit that can be obtained in proton radiography, they already reflect considerable
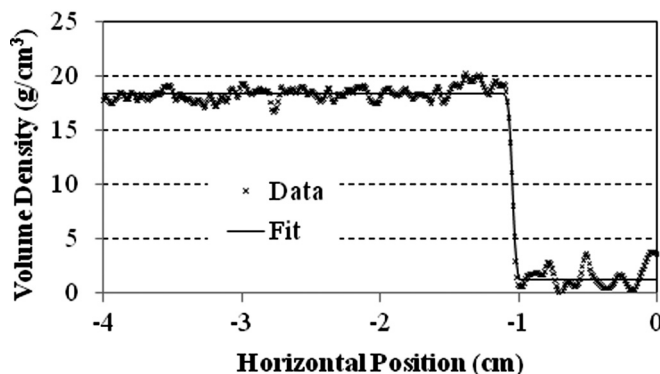

FIG. 11. Fit to the edge of the cavity.

improvement over what can be achieved in X-ray radiography with state of the art flash X-ray machines.[48] These results support previous published conclusions with more detailed objects that the position resolution is about a factor of 4 better and that the effective dose is about a factor of 100 times larger when 24 GeV/*c* protons at the intensities used here are compared to the first axis of DARHT.[49]

[1] D. Hawkins, R. C. Smith, and E. C. Truslow, *Project Y: The Los Alamos Story (The History of Modern Physics, 1800-1950: Volume II)*, (Tomash Publications, Los Angeles, CA, 1983).
[2] G. Seay, "Flash Radiography," Los Alamos Scientific Laboratory Report No. GMX-7-484, 1952.
[3] D. Venable, Phys. Today **17**(12), 19 (1964).
[4] C. L. Mader, T. R. Neal, and R. D. Dick, *LASL Phermex Data* (University of California Press, Berkeley, 1980).
[5] C. Ekdahl, IEEE Trans. Plasma Sci. **30**, 254 (2002).
[6] C. Cavailler, Proc.SPIE **4183**, 23 (2001).
[7] Yongtao Zhao, "Plans for Proton/Ion Radiography at IMP, Lanzhou, China," available at: http://www-aix.gsi.de/conferences/HEPM2009/talks/HEPM-2009-Zhao.pdf, accessed 7 January 2011.
[8] C. Morris, J. W. Hopson, and P. Goldstone, Los Alamos Sci. **30** (2006).
[9] A. Beer, Ann. Phys. Chem. **86**, 78 (1852).
[10] J. H. Hubbell and S. M. Seltzer, "Tables of X-Ray Mass Attenuation Coefficients and Mass Energy-Absorption Coefficients from 1 keV to 20 MeV for Elements Z = 1 to 92 and 48 Additional Substances of Dosimetric Interest," available at: http://www.nist.gov/pml/data/xraycoef/index.cfm, accessed: 1 January 2010.
[11] S. P. Denisov, S. V. Donskov, Y. P. Gorin, R. N. Krasnokutsky, A. I. Petrukhin, Y. D. Prokoshkin, and D. A. Stoyanova, Nucl. Phys. B **61**, 62 (1973).
[12] J. McGill, P. Colestock, F. Neri, L. Rybarcyk *et al.*, "Design Feasibility and Cost Estimate for a Single-Axis, Multipulse Proton Radiography Facility," Los Alamos National Laboratory Report No. (2004).
[13] M. J. Burns, G. J. Caporaso, B. E. Carlsten, Y.-J. Chen, K. P. Chow, E. G. Cook, H. A. Davis, C. A. Ekdahl, W. A. Fawley, C. M. Fortgang, T. P. Hughes, B. R. Trent McCuistian, K. E. Nielsen, H. L. Rutkowski, S. Sampayan, W. L. Waldron, J. A. Watson, G. A. Westenskow, and S. S. Yu, AIP Conf. Proc. **650**, 139 (2002).
[14] Yu. M. Antipov, A. G. Afonin, A. V. Vasilevskii, I. A. Gusev, V. I. Demyanchuk, O. V. Zyat'kov, N. A. Ignashin, Yu G. Karshev, A. V. Larionov, A. V. Maksimov, A. A. Matyushin, A. V. Minchenko, M. S. Mikheev, V. A. Mirgorodskii, V. N. Peleshko, V. D. Rud'ko, V. I. Terekhov, N. E. Tyurin, Yu S. Fedotov, Yu A. Trutnev, V. V. Burtsev, A. A, Volkov, I. A. Ivanin, S. A. Kartanov, Yu P. Kuropatkin, A. L. Mikhailov, K. L. Mikhailyukov, O. V. Oreshkov, A. V. Rudnev, G. M. Spirov, M. A. Syrunin, M. V. Tatsenko, I. A. Tkachenko, and I. V. Khramov, Instrum. Exp. Tech. **53**, 319 (2010).
[15] F. E. Merrill, A. A. Golubev, F. G. Mariam, V. I. Turtikov, and D. Varentsov, Shock Compression Condens. Matter–2009, Parts 1 and 2 **1195**, 667 (2009).
[16] H. Bethe, Ann. Phys. **5**, 325 (1930).
[17] L. Landau, J. Exp. Phys. **8**, 201 (1944).
[18] P. V. Vavilov, Soviet Phys. JETP **5**, 749 (1957).

[19]B. Rossi, *High-Energy Particles* (Prentice-Hall, New Jersey, 1952).

[20]B. Rossi and K. Greisen, Rev. Mod. Phys. **13**, 240 (1941).

[21]G. Molière, Z. Naturforsch. **2a**, 133 (1947).

[22]G. Moliere, Z. Naturforsch. **3a**, 78 (1948).

[23]H. A. Bethe, Phys. Rev. **89**, 1256 (1953).

[24]V. L. Highland, Nucl. Instrum. Meth. **129**, 497 (1975).

[25]G. R. Lynch and O. I. Dahl, Nucl. Instrum. Meth.Phys. Res. **B58**, 6 (1991).

[26]W. E. Frahn and R. H. Venter, Ann. Phys. **24**, 243 (1963).

[27]J. Blatt and V. Weisskopf, *Theoretical Nuclear Physics*. (Dover Publications, Mineola, NY 1991).

[28]K. Nakamura, K. Hagiwara, K. Hikasa, H. Murayama, M. Tanabashi, T. Watari, C. Amsler, M. Antonelli, D. M. Asner, H. Baer, H. R. Band, R. M. Barnett, T. Basaglia, E. Bergren, J. Beringer, G. Bernardi, W. Bertl, H. Bichsel, O. Biebel, E. Blucher, S. Blusk, R. N. Cahn, M. Carena, A. Ceccucci, D. Chakraborty, M.-C. Chen, R. S. Chivukula, G. Cowan, O. Dahl, G. D'Ambrosio, T. Damour, D. de Florian, A. de Gouvea, T. DeGrand, G. Dissertori, B. Dobrescu, M. Doser, M. Drees, D. A. Edwards, S. Eidelman, J. Erler, V. V. Ezhela, W. Fetscher, B. D. Fields, B. Foster, T. K. Gaisser, L. Garren, H.-J. Gerber, G. Gerbier, T. Gherghetta, G. F. Giudice, S. Golwala, M. Goodman, C. Grab, A.V. Gritsan, J.-F. Grivaz, D. E. Groom, M. Grünewald, A. Gurtu, T. Gutsche, H. E. Haber, C. Hagmann, K. G. Hayes, M. Heffner, B. Heltsley, J. J. Hernández-Rey, A. Höcker, J. Holder, J. Huston, J. D. Jackson, K. F. Johnson, T. Junk, A. Karle, D. Karlen, B. Kayser, D. Kirkby, S. R. Klein, C. Kolda, R. V. Kowalewski, B. Krusche, Yu.V. Kuyanov, Y. Kwon, O. Lahav, P. Langacker, A. Liddle, Z. Ligeti, C.-J. Lin, T. M. Liss, L. Littenberg, K. S. Lugovsky, S. B. Lugovsky, J. Lys, H. Mahlke, T. Mannel, A.V. Manohar, W. J. Marciano, A. D. Martin, A. Masoni, D. Milstead, R. Miquel, K. Mönig, M. Narain, P. Nason, S. Navas, P. Nevski, Y. Nir, K. A. Olive, L. Pape, C. Patrignani, J. A. Peacock, S. T. Petcov, A. Piepke, G. Punzi, A. Quadt, S. Raby, G. Raffelt, B. N. Ratcliff, P. Richardson, S. Roesler, S. Rolli, A. Romaniouk, L. J. Rosenberg, J. L. Rosner, C. T. Sachrajda, Y. Sakai, G. P. Salam, S. Sarkar, F. Sauli, O. Schneider, K. Scholberg, D. Scott, W. G. Seligman, M. H. Shaevitz, M. Silari, T. Sjöstrand, J. G. Smith, G. F. Smoot, S. Spanier, H. Spieler, A. Stahl, T. Stanev, S. L. Stone, T. Sumiyoshi, M. J. Syphers, J. Terning, M. Titov, N. P. Tkachenko, N. A. Törnqvist, D. Tovey, T. G. Trippe, G. Valencia, K. van Bibber, G. Venanzoni, M. G. Vincter, P. Vogel, A. Vogt, W. Walkowiak, C. W. Walter, D. R. Ward, B. R. Webber, G. Weiglein, E. J. Weinberg, J. D. Wells, A. Wheeler, L. R. Wiencke, C. G. Wohl, L. Wolfenstein, J. Womersley, C. L. Woody, R. L. Workman, A. Yamamoto, W.-M. Yao, O. V. Zenin, J. Zhang, R.-Y. Zhu, and P. A. Zyla, J. Phys. G: Nucl. Particle Phys. **37**, 075021 (2010).

[29]A. M. Koehler, Science **160**, 303 (1968).

[30]R. Wilson, AIP Conf. Proc., **9**, 578 (1972).

[31]V. W. Steward, IEEE Trans. Nucl. Sci. NS/23, 577 (1976).

[32]D. West, in *7th International Conference on Cyclotrons and their Applications*, edited by W. John (Birkhauser Verlag, Basel, Switzerland, 1975).

[33]R. Martin, M. Foss, J. Moenich and R. Lari, IEEE Trans. Nucl. Sci. NS/22, 1802 (1975).

[34]V. W. Steward and A. M. Koehler, Surg. Neurol. **2**, 283 (1974).

[35]V. W. Steward and A. M. Koehler, Radiology **110**, 217 (1974).

[36]V. W. Steward and A. M. Koehler, Phys. Med. Biol. **18**, 591 (1973).

[37]J. A. Cookson, B. H. Armitage and A. T. Ferguson, Non-Destr. Test. **5**, 225 (1972).

[38]G. A. Ellard, P. T. Gammon, H. S. Helmy, and R. J. W. Rees, Nature **239**, 157 (1972).

[39]A. M. Koehler, AIP Conf. Proc. **9**, 586 (1972).

[40]A. M. Koehler, Phys. Med. Biol. **15**, 181 (1970).

[41]C. T. Mottershead and J. D. Zumbro, in *17th Particle Accelerator Conference*, edited by M. Comyn, M. Craddock, M. Reiser and J. Thomson (IEEE, New York, 1998), pp. 1397–1399.

[42]Bergoz Instrumentation, "Bergoz Instrumentation, Espace Allondon Ouest 01630 Saint Genis Pouilly, France," available at http://www.bergoz.com/index.php?optio=com_content&view=frontpage&Itemid=1, accessed: 7 December 2010.

[43]JAI A/S - Denmark, Copenhagen, Denmark, "*TM-1040 rogressive Scanning High Resolution Camera*", url: http://www.jai.com/SiteCollectionDocuments/Camera_Solutions_Manuals/TM-Manuals/Manual_TM-1040.pdf, accessed: February 2011.

[44]C. L. Morris and A. Saunders, "NewDisplay", Report No. LA-CC-04-110, 2004.

[45]J. Zumbro, Nucl. Instrum. Meth. Phys. Res. B **246**, 479 (2006).

[46]J. D. Zumbro, "Angle-cuts for the Brookhaven proton radiography experiments E955 and E963 calculated with MCNP™ (U)," Los Alamos national Laboratory, Report No. LA-UR-05-7370, 2005.

[47]W. Press, B. Flannery, S. Teukolsky, and W. Vetterling, *Numerical Recipes in Fortran*, 2nd ed. (Cambridge University Press, Cambridge, 1992).

[48]G. Cunningham and C. Morris, Los Alamos Sci. **28**, 76 (2003).

[49]C. L. Morris, K. R. Alrick, K. L. Buescher, D. J. Cagliostro, D. J. Clark, D. A. Clark, G. S. Cunningham, C. J. Espinoza, E. N. Ferm, R. Gallegos, S. D Gardner, J. J. Gomez, N. T. Gray, G. A. Greene, A. L. Hanson, G. W. Hart, M. Y. Hockaday, G. E. Hogan, N. S. Khalsa, N. S. King, K. K. Kwiatkowski, R. P. Liljestrand, A. R. Mathews, J. B. McClelland, B. Montoya, D. V. Morgan, K. B. Morley, C. T. Mottershead, K. H. Mueller, M. M. Murray, P. D. Pazuchanics, J. E. Pearson, R. A. Pelak, A. Saunders, J. Scaduto, S. F. Sterbenz, R. T. Thompson, T. W. Tunnell, K. R. Vixie, S. A. Watson, A. Whiteson, and M. D. Wilke, Defense Res. Rev. **11**, 51 (2004).